Supporting Information

Engineering sub-2 nm ultrasmall high-entropy alloy nanoparticles with extremely superior performance for hydrogen evolution catalysis

Feng et al.

Supplementary Figures:

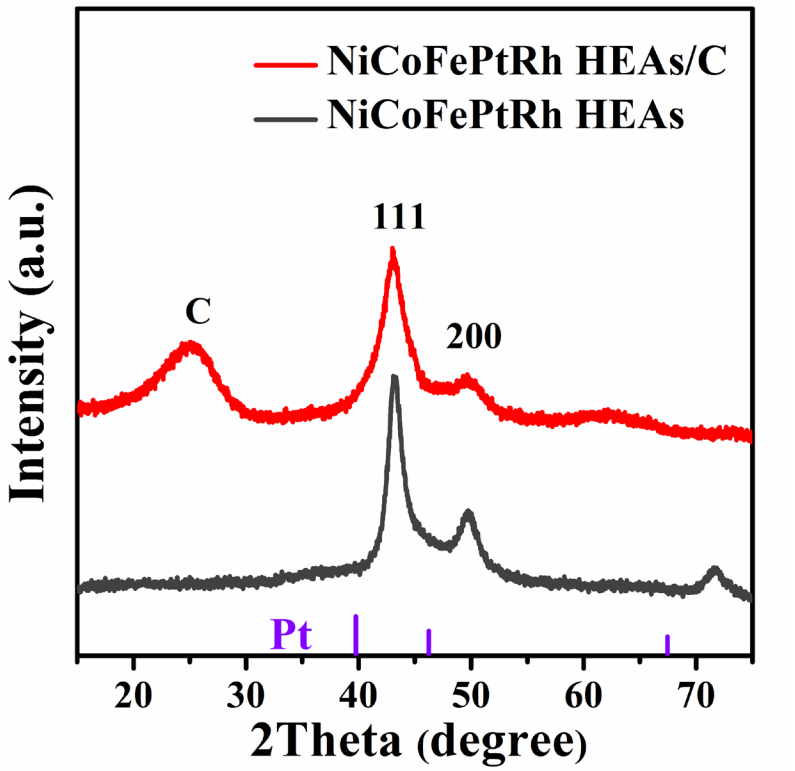

Supplementary Figure 1. Powder XRD patterns of NiCoFePtRh high-entropy alloys (HEAs) with carbon supports (catalyst load is 25 wt% in theory) and without carbon supports. The standard XRD pattern of Pt (JCPDS 03-065-2868) is also shown at the base for comparison.

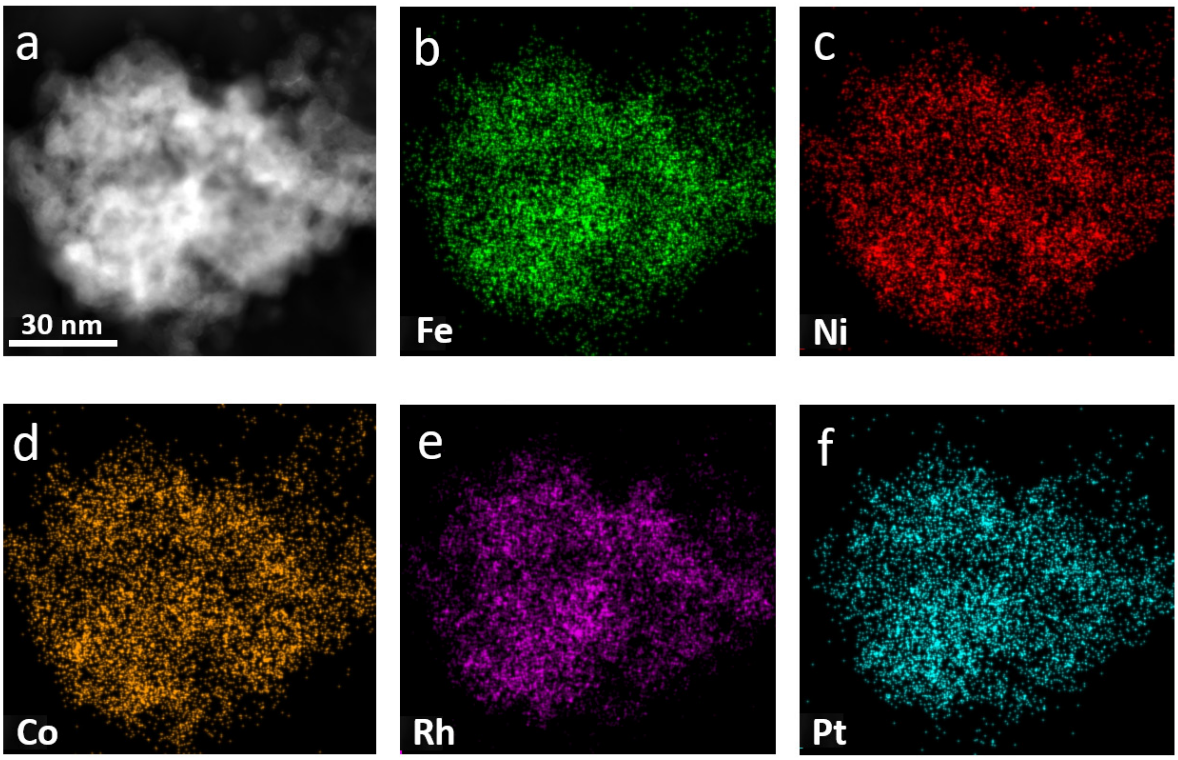

Supplementary Figure 2. a High-angle annular dark-field scanning transmission electron microscopy (HAADF-STEM) image of NiCoFePtRh HEAs, showing a significant agglomeration. Corresponding energy dispersive spectroscopy (EDS) elemental mapping of (**b**) Fe, (**c**) Ni, (**d**) Co, (**e**) Rh, and (**f**) Pt.

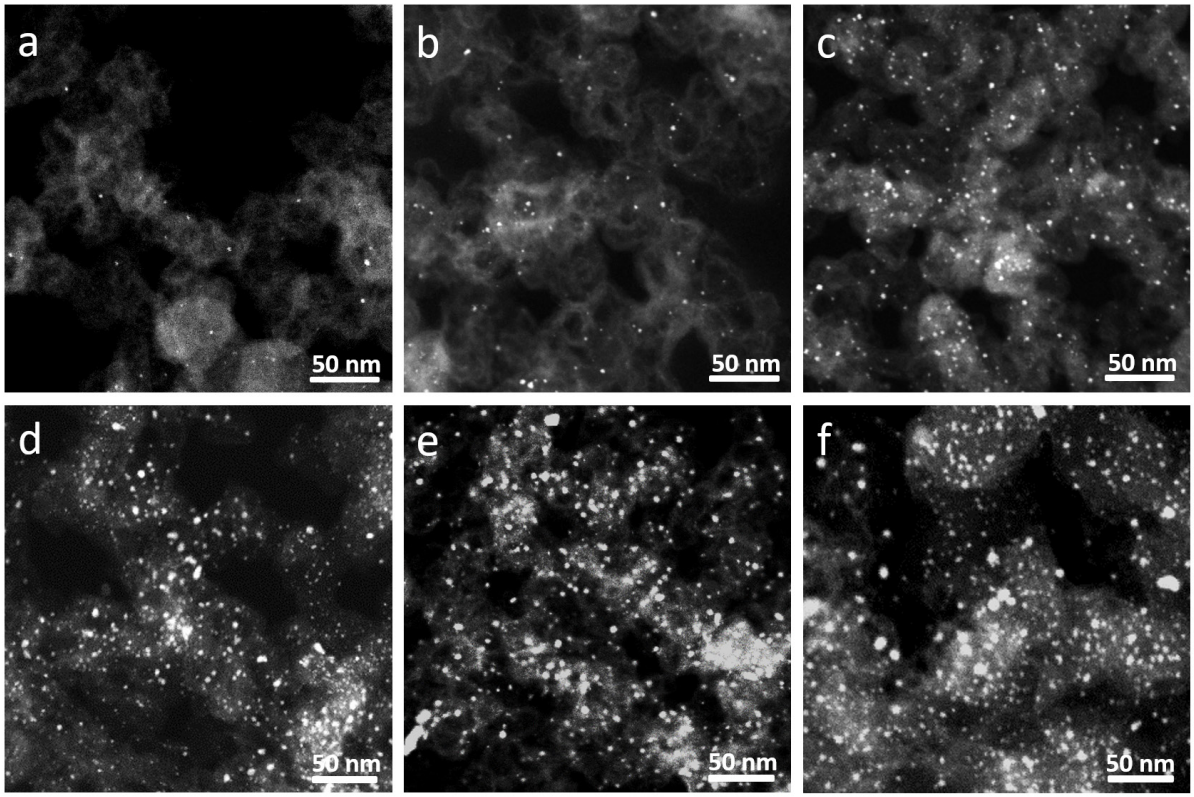

Supplementary Figure 3. HAADF-STEM images of the NiCoFePtRh HEA NPs with different loadings in theory on the carbon supports. a 1 wt%. b 2 wt%. c 5 wt%. d 10 wt%. e 20 wt%. f 25 wt%. As the loading increases, the size of the particles increases. When the loading exceeds 10 wt%, the particles begin to grow and agglomerate obviously, which is also confirmed by the sharp (111) peaks at 43.2° below. In contrast, 5 wt% loading has the optimal particle dispersion and ultrasmall particle size. So, 5 wt% loading is the most appropriate in this work. 5 wt% HEA/C is the us-HEA/C mentioned in this work.

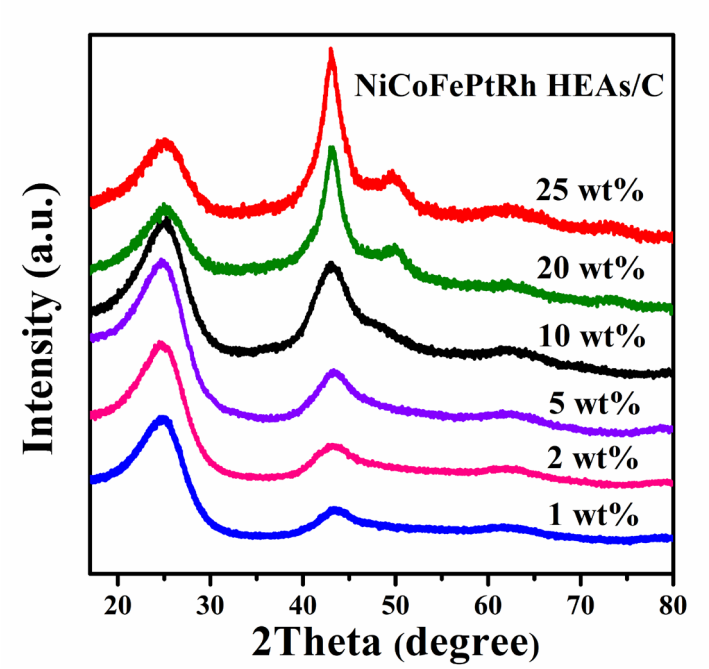

Supplementary Figure 4. Powder XRD patterns of the NiCoFePtRh HEAs/C with different loadings.

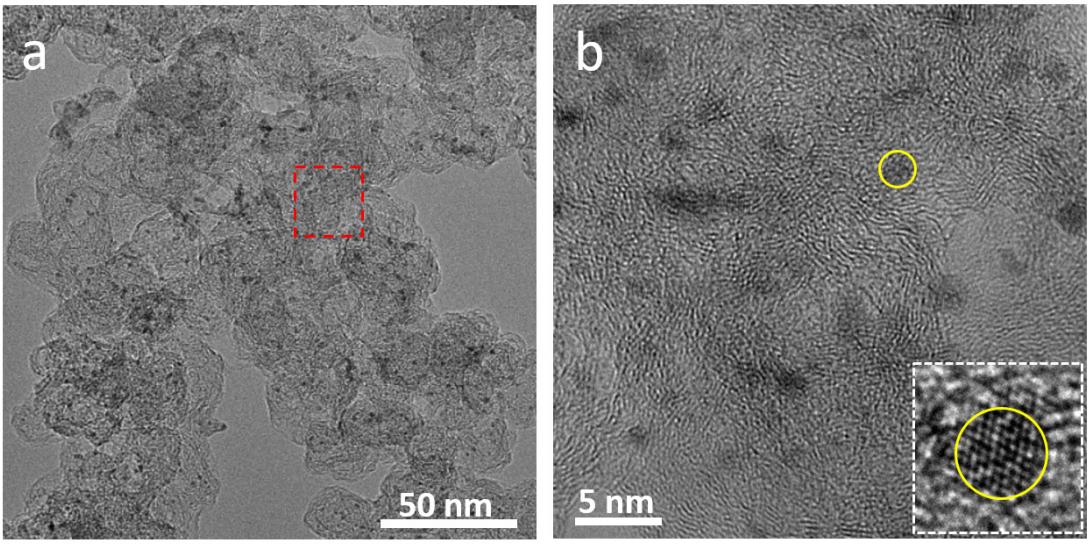

Supplementary Figure 5. TEM image (**a**) and high-magnification TEM image (**b**) of us-HEA NPs loaded on the carbon support.

Supplementary Table 1. A list of the high-entropy alloys (HEAs) reported previously.

HEAs	Size (nm)	Synthetic Method	Electrocatalysis (Yes/No)	Ref.
HEA pillars	70-100	Ion beam milling	No	*Nano Lett.*, **2017**, 17, 1569-1574
PtFeCoNiCu NPs PtPdIrRhRu NPs	~ 5.3 ~ 3.3	Carbothermal shock	No	*Science*., **2018**, 359, 1489-1494
PH-HEAs	> 1000	Arc melting	No	Nat. Commun., **2018**, 9, 4063
CoMoFeNiCu NPs	~ 22	Carbothermal shock	Yes (NH_3 decomposition)	*Nat. Commun.*, **2019**, 10, 4011
CrMnFeCoNi films CrFeCoNiPd films	> 100	Arc melting	No	*Nature.*, **2019**, 574, 223-227
us-HEA NPs	~ 1.68	Chemical co-reduction	Yes (HER)	This work

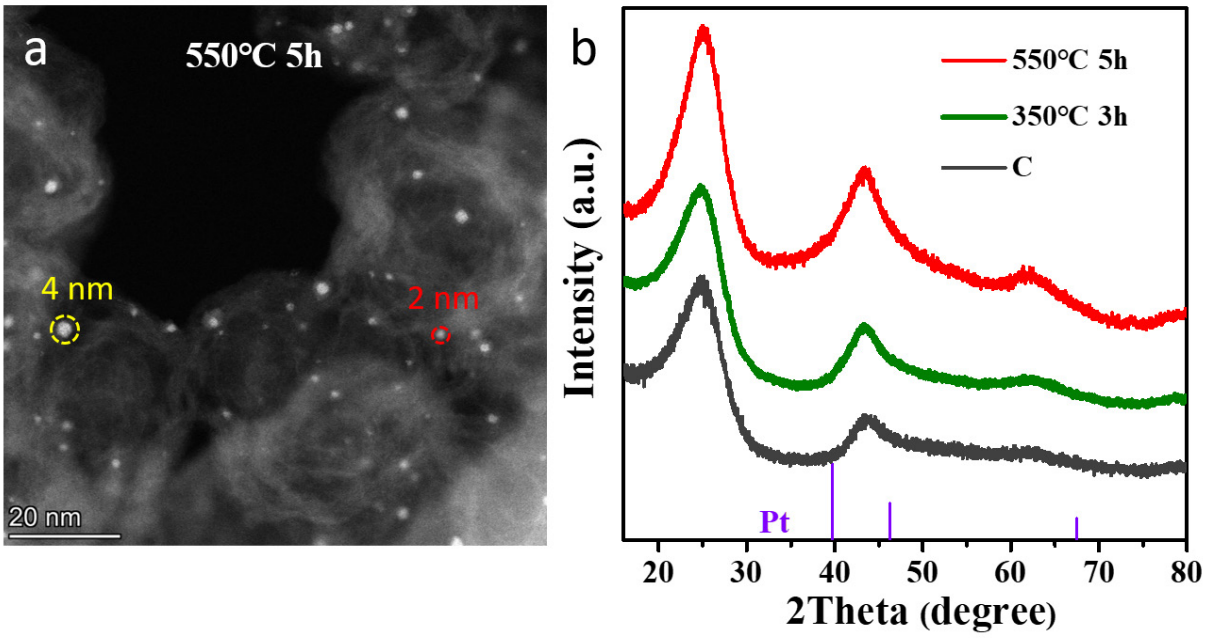

Supplementary Figure 6. HAADF-STEM image (**a**) and XRD pattern (**b**) of us-HEA NPs annealed in a H_2/Ar flow at 550 ℃ for 5 h, showing no obvious change compared with those of the sample treated at 350 ℃ for 3 h.

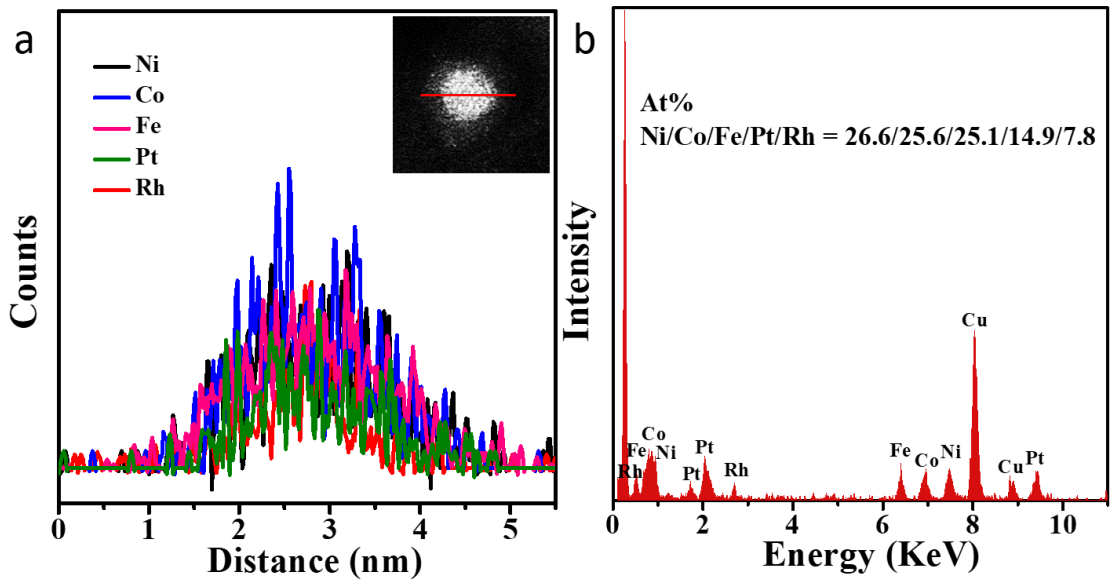

Supplementary Figure 7. a Line scanning profiles of a single us-HEA NP, indicating that all five elements homogeneously disperse throughout the NP. **b** EDS spectrum of the us-HEA NP shown in (**a**).

Supplementary Table 2. The ICP analysis of the us-HEA/C, which is roughly in accordance with the compositions of the nanoparticle in Supplementary Fig. 7b.

Element	At %
Ni	26.8
Co	26.1
Fe	25.6
Pt	13.6
Rh	7.9

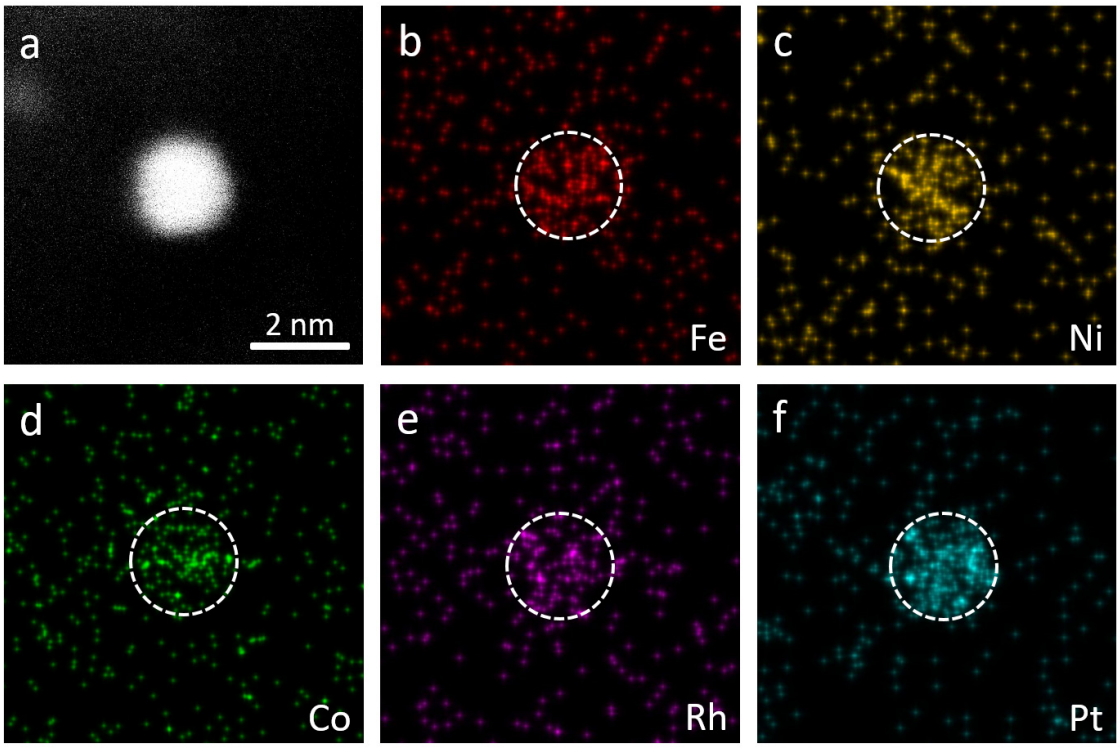

Supplementary Figure 8. The elemental maps of a 2 nm NiCoFePtRh NP. The five metal elements in this nanoparticle are seriously damaged during the elemental map characterization. So larger nanoparticles were selected to obtain clear elemental maps in this work.

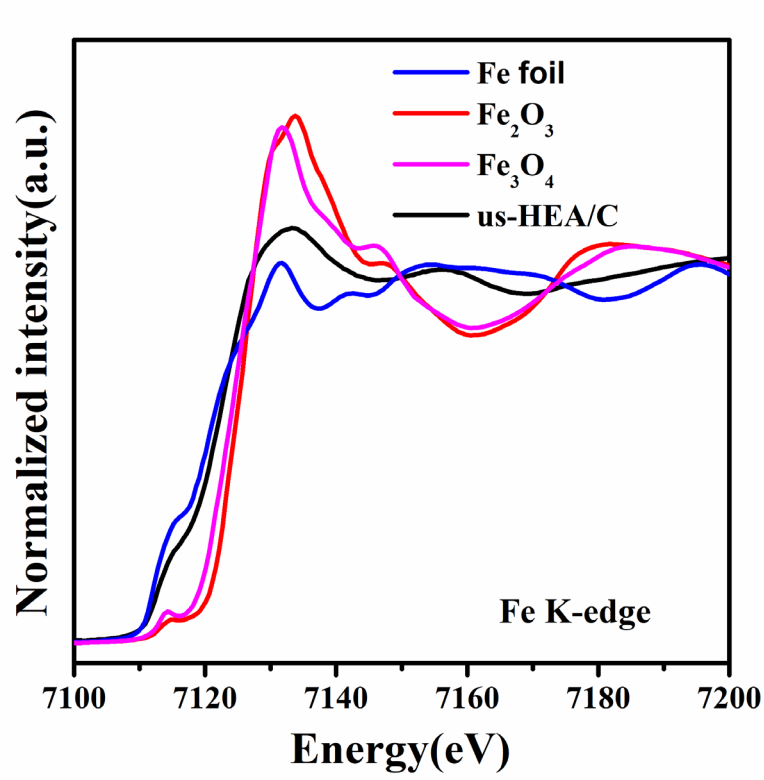

Supplementary Figure 9. X-ray absorption near edge structure (XANES) spectra for the Fe K-edge.

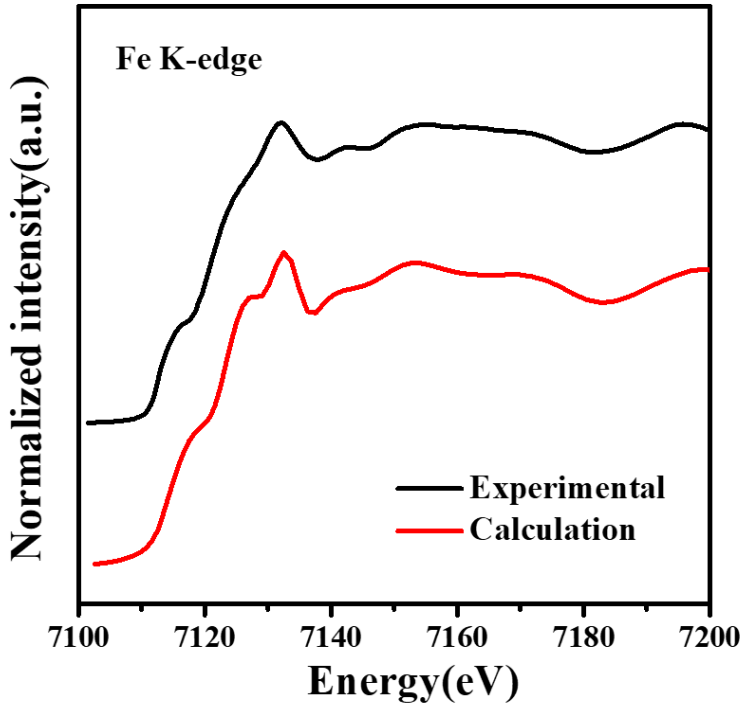

Supplementary Figure 10. Comparison of the experimental Fe K-edge XANES in bcc iron and the theoretical one.

The XANES spectrum of the standard Fe foil with bcc structure has been reproduced successfully to find the appropriate non-structure parameters, including the type of potential, Fermi level, core hole and so on. The theoretical full potential calculation has been performed for the Fe K-edge XANES by using the Feff8.2 code (*Phys. Rev. B: Condens. Matter Mater. Phys*., 1998, 58, 7565).

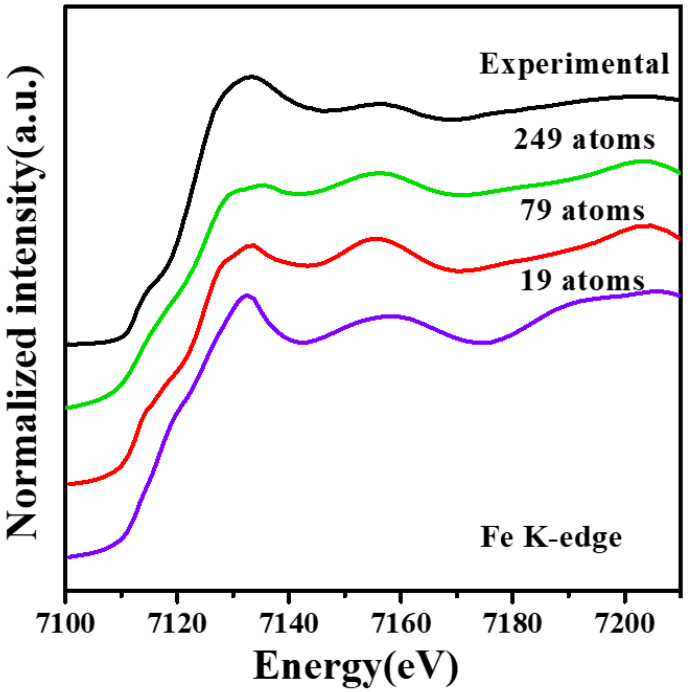

Supplementary Figure 11. Comparison of the experimental Fe K-edge XANES of the as-synthesized us-HEA/C and the theoretical spectra for different sizes. The cluster of 249 atoms around Fe represents the Fe is in bulk, while the Fe in the 19-atoms cluster is on (sub-) surface.

The theoretical spectra of Fe K-edge XANES with the different cluster sizes have been reproduced based on the solid-state structure of fcc. The intensity of the pre-edge peak, which is a typical fingerprint for a metal element, becomes weaker with decease of the size, while the main peak intensity is stronger. This kind of XANES feature evolution with the size decrease is a little similar the oxidation effect, especially for the ultrasmall cluster.

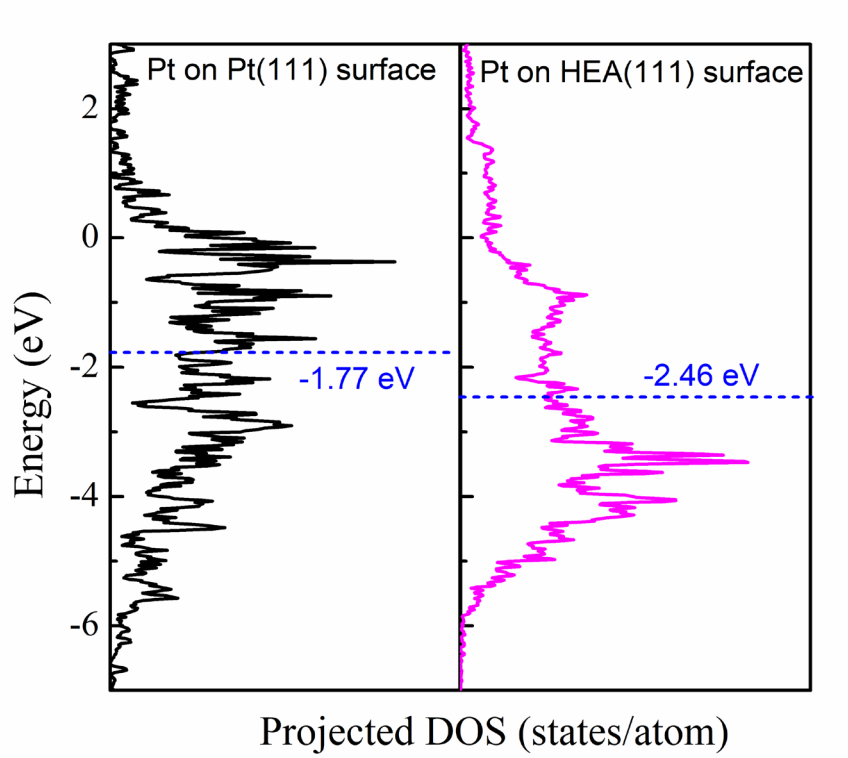

Supplementary Figure 12. Projected density of states (DOS) of the *d*-band for the surface Pt atoms in the pure Pt(111) and us-HEA(111) slab system. The horizontal dashed lines indicate the calculated *d*-band centre.

The projected density of states (DOS) of the *d*-band for the surface Pt atoms in us-HEA(111) slab differ from that of pure Pt(111) slab, indicating that the *d*-band of surface Pt atoms is tuned by the alloying effects of the us-HEA(111) slab. The centre of the *d*-band dropped by 0.69 eV relative to the pure Pt(111) slab. The downshift of the *d*-band centre relieves the over-binding of hydrogen on the surface, resulting in weaker H adsorption, thus shifting the hydrogen-adsorption free energies (ΔG_{H^*}) towards the optimal value.

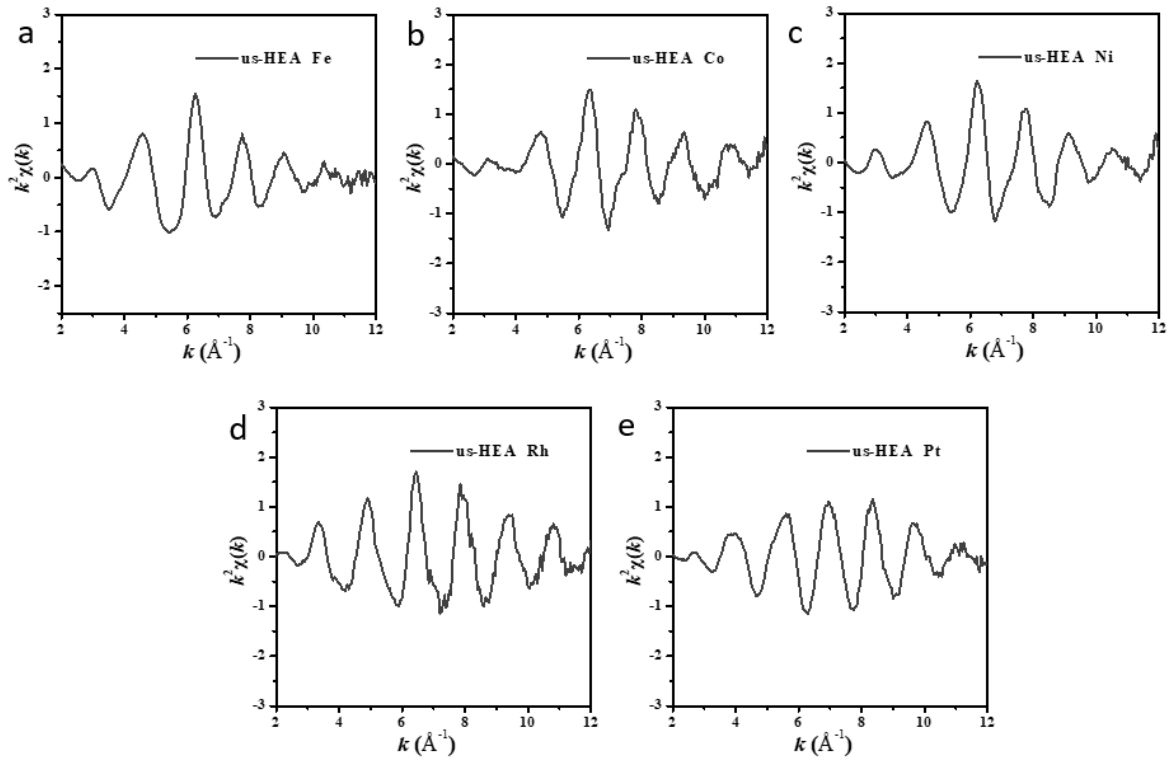

Supplementary Figure 13. Experimental k^2-weighted EXAFS oscillations of the as-prepared us-HEA/C at Fe, Co, Ni, Rh K-edge and Pt L_3-edge.

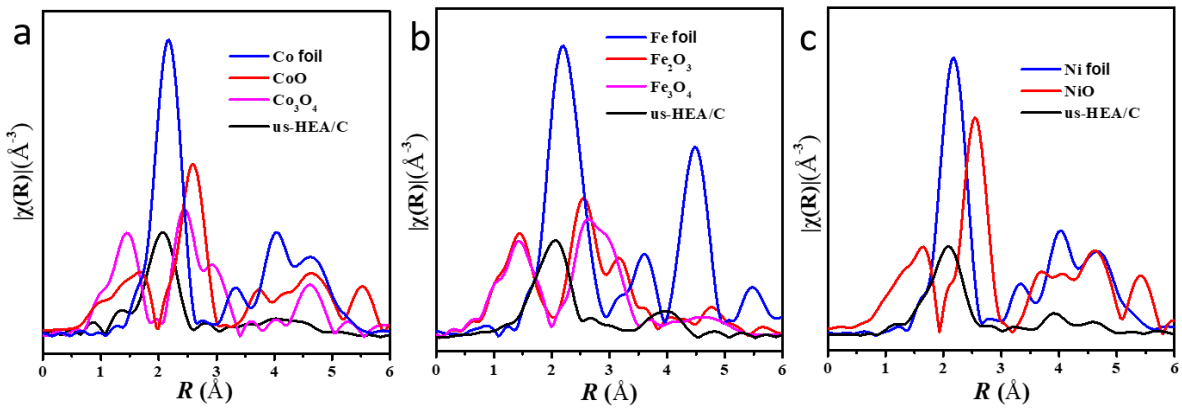

Supplementary Figure 14. Extended XAFS spectra of us-HEA/C for Co K-edge (**a**), Fe K-edge (**b**), and Ni K-edge (**c**).

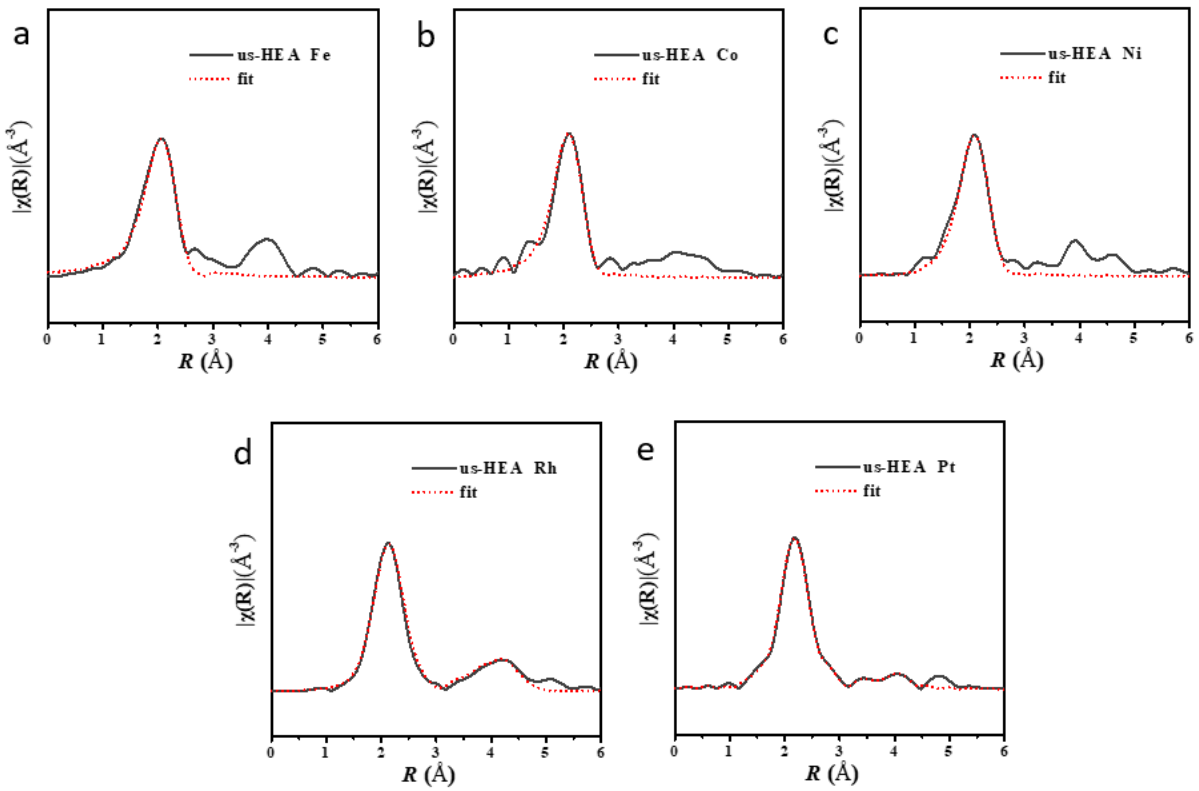

Supplementary Figure 15. Comparison of the experimental k^2-weighted EXAFS and the fitting curves in the R space for the as-prepared us-HEA/C at Fe, Co, Ni, Rh K-edge and Pt L_3-edge.

The EXAFS was fitted by using the IFEFFIT software (*J. Synchrotron Rad.*, 2005, 12, 537-541). Because of the low loading content and the ultrasmall size of the us-HEA NPs, the EXAFS spectra in the R space only present a dominant peak at ca. 2.07 Å for Fe, Co and Ni, 2.13 Å for Rh and 2.18 Å for Pt (without phase corrections), which is ascribe to the nearest neighbored shell around the absorbed center. The FT-EXAFS of the higher shells is weak and hard to be distinguished. Therefore, only the local atomic arrangement of the first shell achieved from the EXAFS is more reliable and accurate for our ultrasmall particles. In the fits, the scattering amplitude and phase were calculated by Feff8.2 code (*Phys. Rev. B: Condens. Matter Mater. Phys.*, 1998, 58, 7565) with the fcc structure as the initial model. Due to the limitation of the statistical average of the EXAFS technique, the different metallic elements (Me: Fe, Co, Ni, Rh and Pt) around the absorbed center in the same position were represented by Co in the fits. In fact, the scattering amplitude and phase of Fe, Co and Ni (adjacent elements), which are of the majority composition elements in the HEA NPs, is almost identical. So this fitting strategy only leads to much limited errors.

In the fits, the k-range data of 2-12 $Å^{-1}$ and the r-range of 1.6-2.8 Å give 7 independent points for the first shell fits of Fe, Co and Ni K-edge FT-EXAFS, while the number of

variable parameters (CN, R, σ^2 and ΔE_0) is 4. For the Rh K-edge, the r-range of 1.6-4.8 gives 20 independent points and 16 variable parameters have been fitted until the fourth shells. For the Pt L_3-edge, the r-range of 1.6-3.8 Å gives 13 independent points and 12 variable parameters have been fitted until the third shells, due to the weak signals in the higher range of FT curve.

Supplementary Table 3. EXAFS fitting results for the HEA nanoparticles at Fe, Co, Ni and Rh K-edge and Pt L_3-edge.

metals	*pair*	*N*[a]	*R* (Å)	σ^2 ($\times 10^{-3}$ Å^2)[b]	S_0^2 *(eV)*
Fe	Fe-Me	8.6 ± 1.0	2.50 ± 0.02	13.6 ± 1.5	0.80
Co	Co-Me	8.5 ± 1.0	2.50 ± 0.02	13.2 ± 1.3	0.77
Ni	Ni-Me	8.5 ± 1.0	2.51 ± 0.02	13.0 ± 1.3	0.81
Rh	Rh-Me	8.4 ± 1.0	2.59 ± 0.02	8.4 ± 0.9	0.90
	Rh-Fe/Co/Ni	2.7 ± 0.3	3.68 ± 0.04	18.0 ± 2.0	
	Rh-Pt	1.2 ± 0.3	3.84 ± 0.04	3.0 ± 0.5	
Pt	Pt-Me	8.4 ± 1.0	2.61 ± 0.02	8.8 ± 1.0	0.75
	Pt-Fe/Co/Ni	3.2 ± 0.6	3.69 ± 0.04	16.0 ± 2.0	
	Pt-Rh	0.8 ± 0.2	3.85 ± 0.04	14.0 ± 2.0	

[a] Product of S_0^2 and the coordinator number in a given shell determines its FT amplitude. Here the value of S_0^2 is determined by fitting the EXAFS spectra of the standard metal foils.

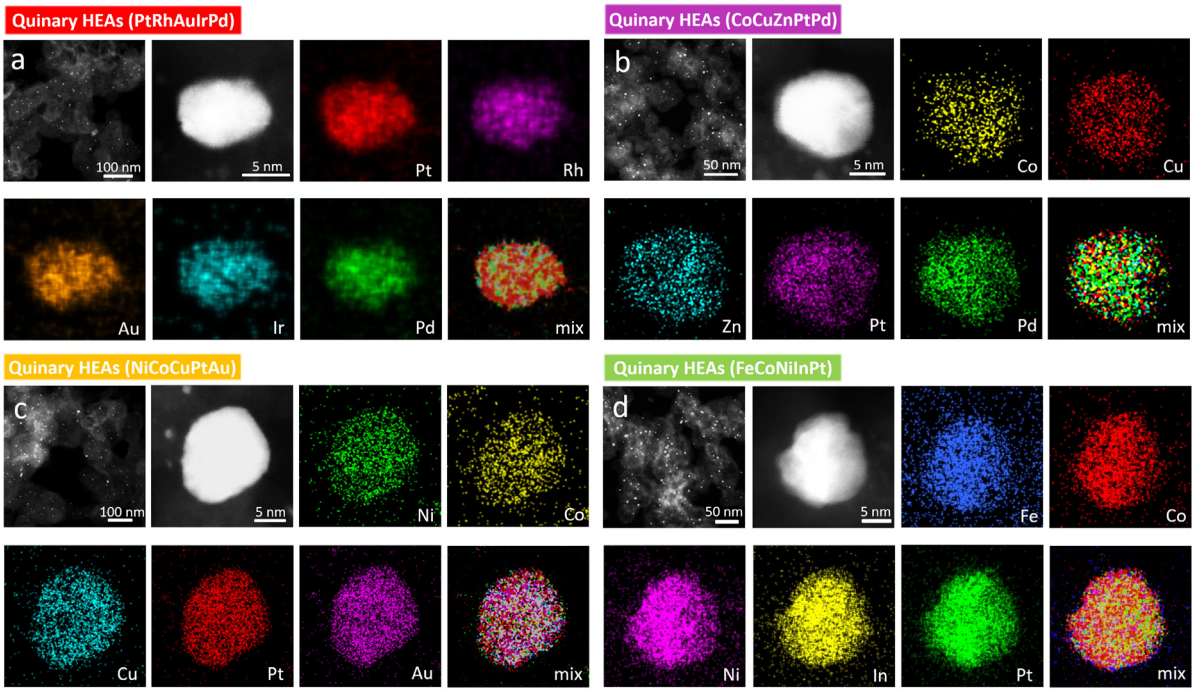

Supplementary Figure 16. The HAADF-STEM images and elemental maps of as-prepared quinary HEAs. **a** PtRhAuIrPd. **b** CoCuZnPtPd. **c** NiCoCuPtAu. **d** FeCoNiInPt.

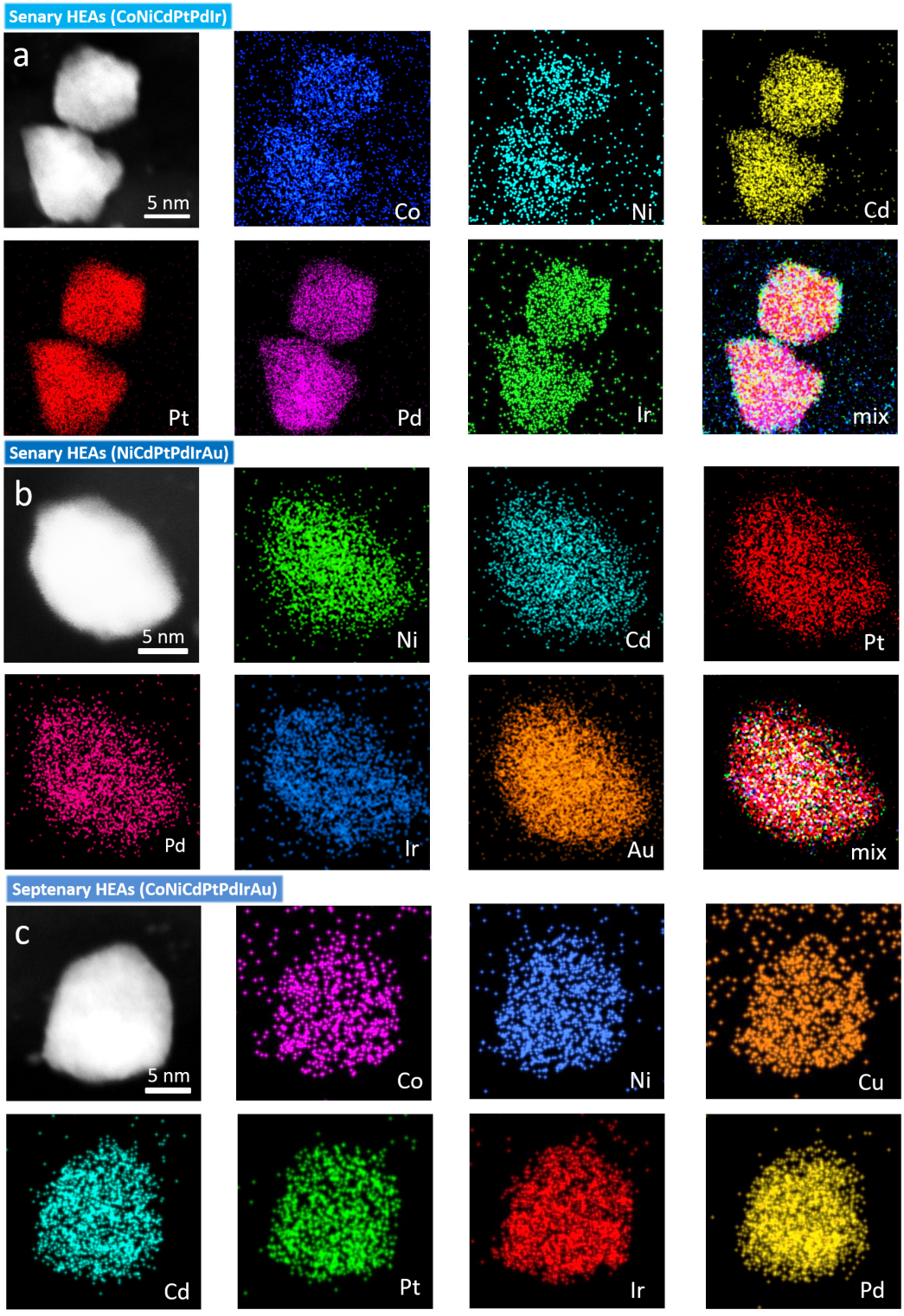

Supplementary Figure 17. The elemental maps of as-prepared senary and septenary HEAs. a CoNiCdPtPdIr. b NiCdPtPdIrAu. c CoNiCdPtPdIrAu.

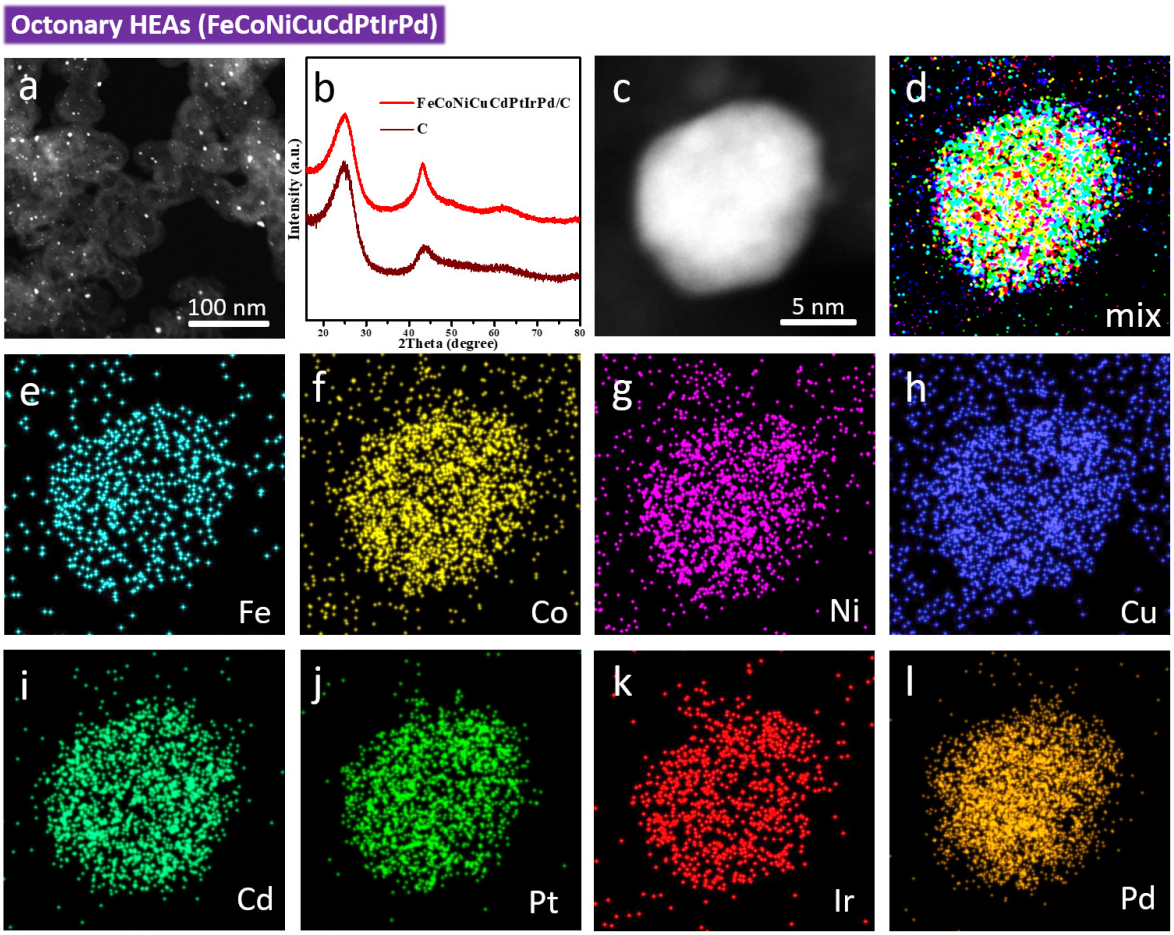

Supplementary Figure 18. The HAADF-STEM image (a), powder XRD pattern (b), elemental maps (c-l) of as-prepared octonary HEA (FeCoNiCuCdPtIrPd). The HAADF-STEM image shows that the HEA NPs are uniformly dispersed on the carbon supports. The single and obvious (111) peak at 43.3° of XRD reveals that the nanoparticles in the octonary HEAs form homogeneous alloys and the HEAs are successfully synthesized.

Supplementary Table 4. Comparison of the geometric area activities of the advanced noble metal catalysts reported in the literatures for hydrogen evolution reaction in 0.5 M H_2SO_4. The iR refers to iR compensation.

Catalyst	Noble metal loading amount	Overpotential at 10 mA cm^{-2} (mV)	Overpotential at 10 mA cm^{-2} (mV) (iR)	Ref.
Pt ALD	3.5 ug cm^{-2}	47	~	*Nat. Commun.*, **2017**, 8, 1074
Pt_1/OLC	1.377 ug cm^{-2}	38	~	*Nat. Energy*., **2019**, 4, 512-518
$Mo_2TiC_2T_x$-Pt_{SA}	12 ug cm^{-2}	30	~	*Nat. Catal*., **2018**, 1, 985-992
ALD50Pt/N-doped Gr	1.61 ug cm^{-2}	38	~	*Nat. Commun.*, **2016**, 7, 13638
L-Ag	200 ug cm^{-2}	32	~	*Nat. Catal*., **2019**, 2, 1107-1114
Pt-MoS_2	27 ug cm^{-2}	80	~	*Nat. Commun*., **2013**, 4, 1444
Pt@PCM	11.2 ug cm^{-2}	105	~	*Sci. Adv*., **2018**, 4, eaao6657
IrNiTa	8.14 ug cm^{-2}	99	~	*Adv. Mater.*, **2020**, 32, 1906384
Pt ML/Au NF	0.55 ug_{Pt} cm^{-2}	100	~	*Sci. Adv.*, **2015**, 1, e1400268
Li-PPS NDs	15.53 ug cm^{-2}	~	91	*Nat. Catal*., **2018**, 1, 460-468
1% PtW_6O_{24}/C	~	~	22	*Nat. Commun.*, **2020**, 11, 490
Ru@C_2N	285 ug cm^{-2}	~	22	*Nat. Nanotech*., **2017**, 12, 441-446
us-HEA/C	**0.8224 ug cm^{-2}**	**27**	**20**	**This work**

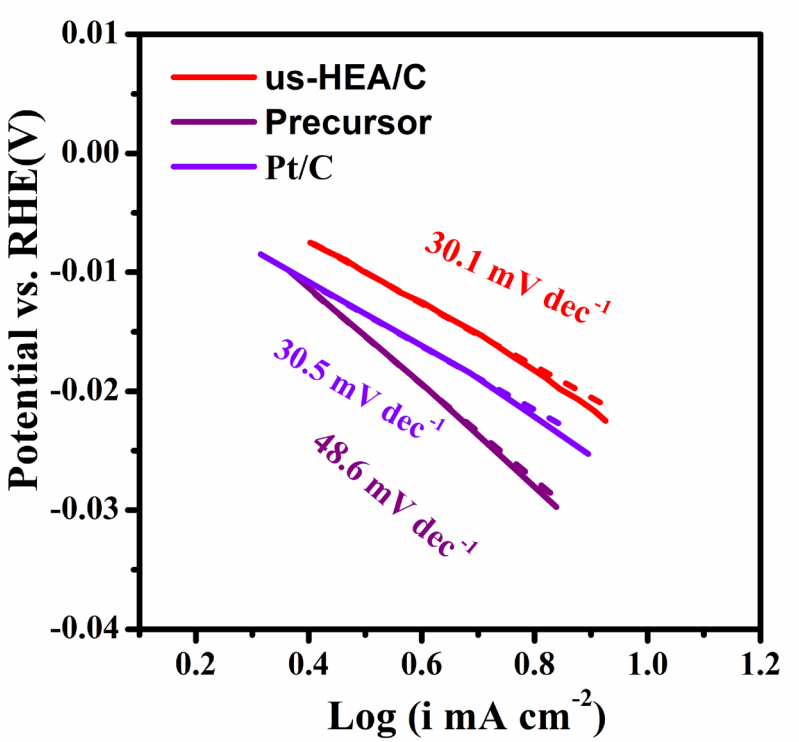

Supplementary Figure 19. Tafel plots of the geometric area activities of the us-HEA/C, the precursor, and commercial Pt/C in 0.5 M H_2SO_4 solution. Tafel slope was obtained from Tafel equation $\eta = b \log j + c$, where η is the potential, b is the Tafel slope, j is the current density, and c is the intercept.

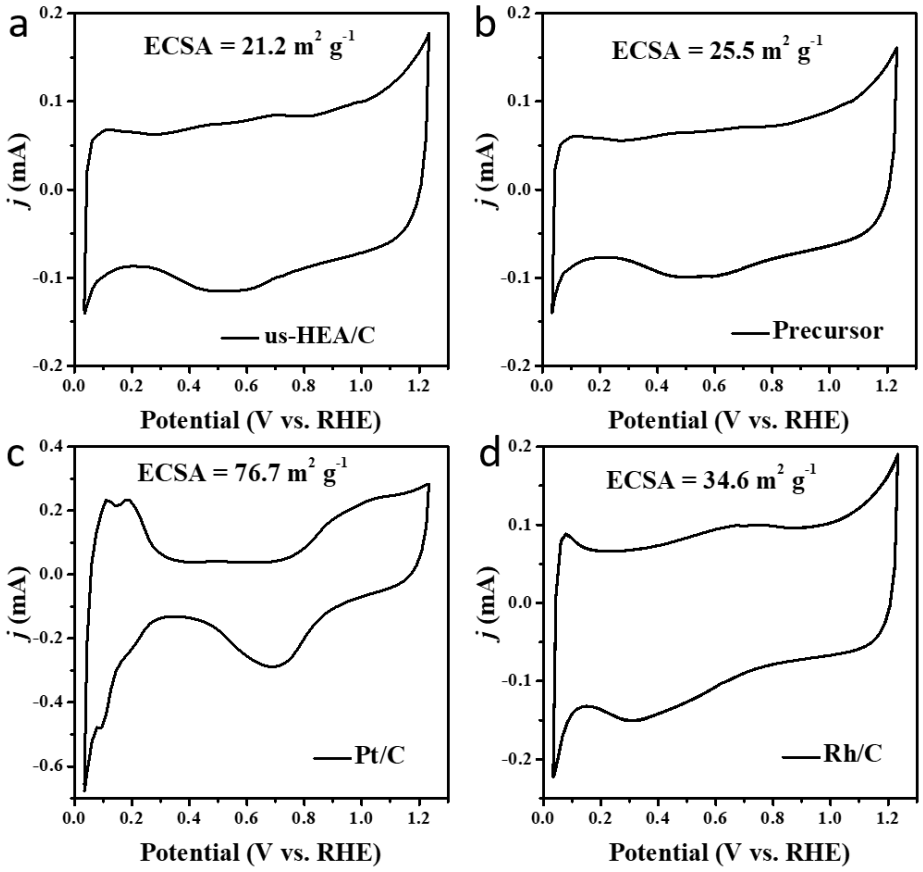

Supplementary Figure 20. Electrochemically active surface areas (ECSAs) of us-HEA/C (**a**), precursor (**b**), commercial Pt/C (**c**), and commercial Rh/C (**d**), estimated via the hydrogen absorption-desorption regions of the corresponding CV curves, and calculated by the equation ECSA (m^2 g^{-1}) = Q_{upd}/(210**m*)*10^8. Q_{upd} is the value of integral area of desorption peak over scanning speed and *m* is metal loading on working electrode. Q_{upd}, 210, and *m* are in units of C, μC cm^{-2} and μg, respectively. The CV curves were measured at a scanning rate of 50 mV s^{-1} in N_2-saturated 0.5 M H_2SO_4 solution.

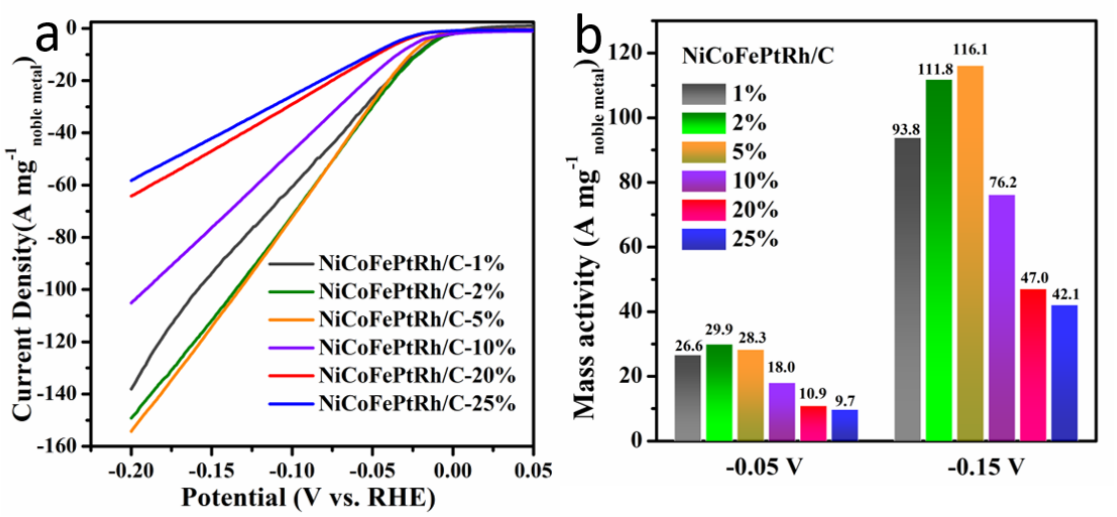

Supplementary Figure 21. Mass activities of the NiCoFePtRh HEAs/C with different loading for HER in 0.5 M H_2SO_4 solution. a Polarization curves. b Quantitative comparisons of the mass activities at different potentials. 5 wt% NiCoFePtRh HEA/C is the us-HEA/C mentioned in this work.

Supplementary Table 5. Comparison of the mass activities and TOFs of advanced noble metal catalysts reported in the recent literatures for hydrogen evolution reaction.

Catalysts	Electrolyte	Mass Activity at -0.05 V (A mg^{-1})	TOFs (at x overpotential) (s^{-1})	Ref.
Pt-Ru dimers	0.5 M H_2SO_4	23.10	~	*Nat. Commun.*, **2019**, 10, 4936
Pt-GT-1	0.5 M H_2SO_4	19.85	7.22 (18 mV)	Nat. Energy., **2018**, 3, 773-782
Pt_1/hNCNC	0.5 M H_2SO_4	19.00	7.67 (20 mV)	*Nat. Commun.*, **2019**, 10, 1657
1% PtW_6O_{24}/C	0.5 M H_2SO_4	13.10	33.35 (100 mV)	*Nat. Commun.*, **2020**, 11, 490
Pt_1/OLC	0.5 M H_2SO_4	9.75	40.78 (100 mV)	*Nat. Energy*., **2019**, 4, 512-518
AL-Pt/Pd_3Pb	0.5 M H_2SO_4	7.83	~	*J. Am. Chem. Soc*., **2019**, 141, 19964-19968
$RuIrO_x$	0.5 M H_2SO_4	6.50	~	*Nat. Commun.*, **2019**, 10, 4875
$Mo_2TiC_2T_x$-Pt_{SA}	0.5 M H_2SO_4	5.39	~	*Nat. Catal*., **2018**, 1, 985-992
Pt_3Ni_2NWs-S/C	0.5 M H_2SO_4	2.16	~	*Nat. Commun*., **2017**, 8, 14580
L-Ag	0.5 M H_2SO_4	0.18	~	*Nat. Catal*., **2019**, 2, 1107-1114
RuSi	0.5 M H_2SO_4	0.04	~	*Angew. Chem. Int. Ed*., **2019**, 58, 11409-11413
IrHNC	0.5 M H_2SO_4	~	4.21 (25 mV)	*Nat. Commun.*, **2019**, 10, 4060
Li-PPS NDs	0.5 M H_2SO_4	~	1.60 (140 mV)	*Nat. Catal*., **2018**, 1, 460-468
Ru@C_2N	0.5 M H_2SO_4	~	0.67 (25 mV)	*Nat. Nanotech*., **2017**, 12, 441-446
IrNiTa	0.5 M H_2SO_4	~	19.30 (100 mV)	*Adv. Mater.*, **2020**, 32, 1906384
us-HEA/C	0.5 M H_2SO_4	28.30	7.93 (18 mV) 8.61 (20 mV) 11.01 (25 mV) 75.40 (100 mV)	This work

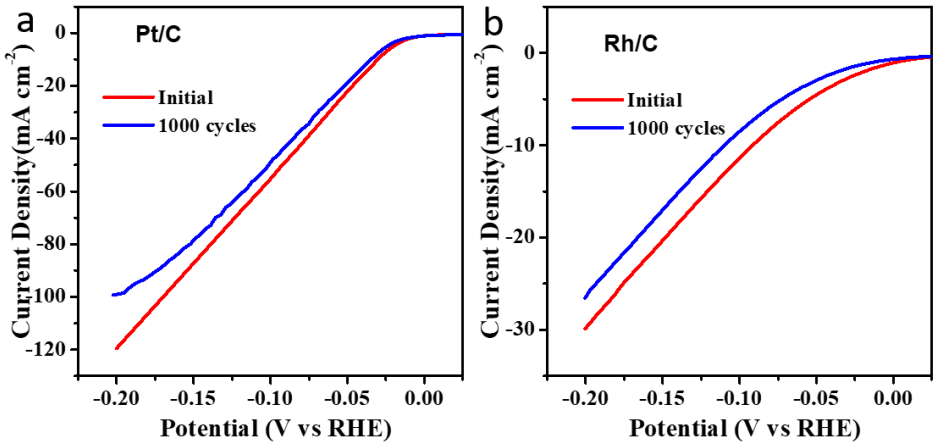

Supplementary Figure 22. LSV curves of commercial Pt/C (**a**) and commercial Rh/C (**b**) before and after 1000 potential cycles in 0.5 M H_2SO_4 solution from 0.1 to -0.2 V (vs RHE), showing conspicuous negative shifts.

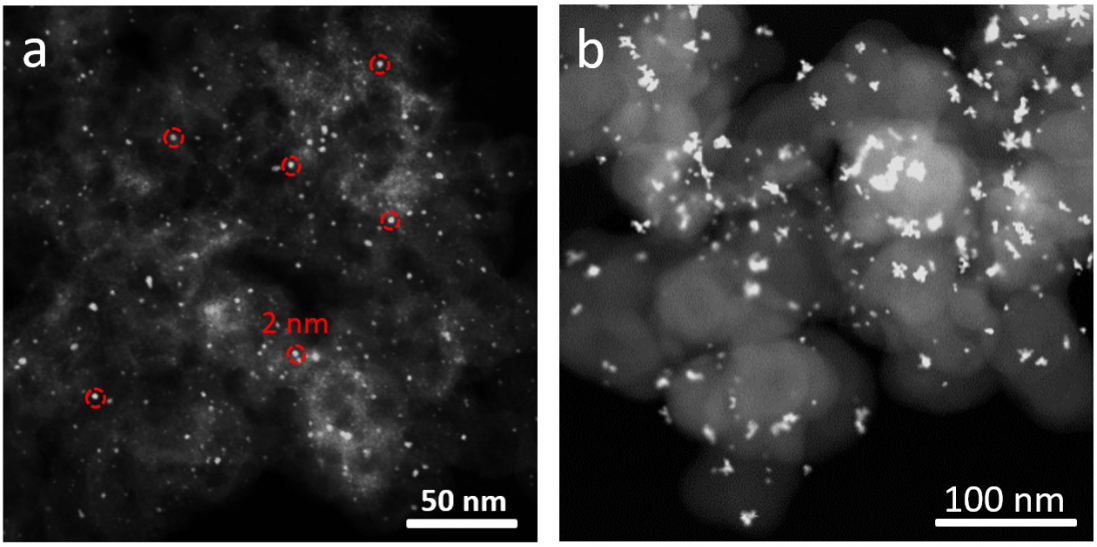

Supplementary Figure 23. HAADF-STEM images of us-HEA/C (**a**) and Pt/C (**b**) after potential cycles tests, showing us-HEA/C has no obvious particle growth and agglomerations, while the Pt/C agglomerates severely.

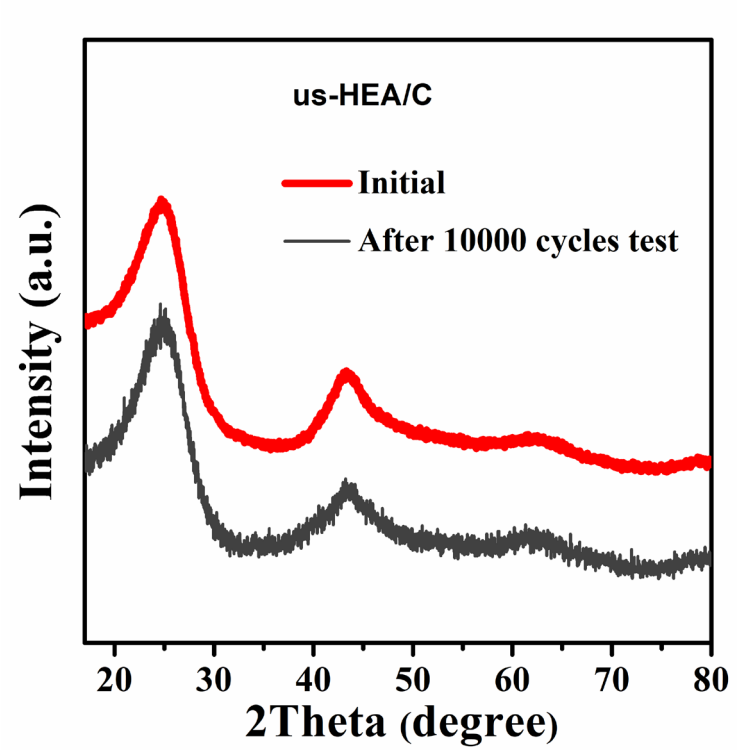

Supplementary Figure 24. XRD patterns of us-HEA/C nanoparticle before and after the accelerated degradation test, showing almost no change.

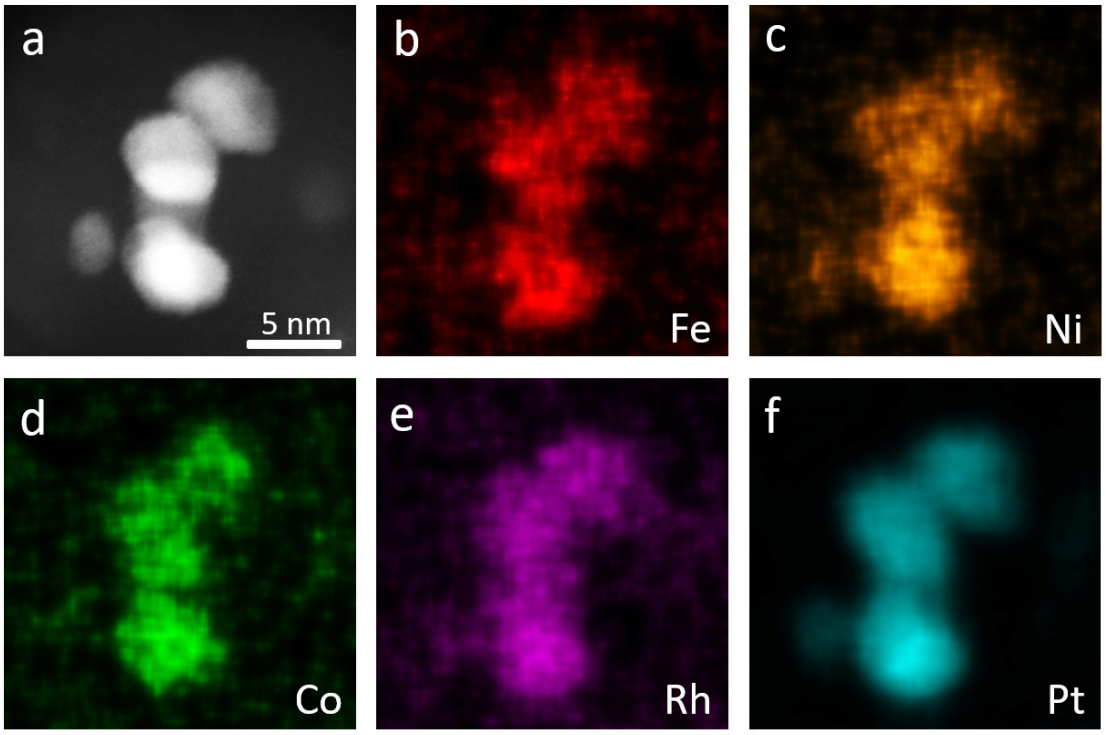

Supplementary Figure 25. Elemental distributions of us-HEA/C after the accelerated degradation test, revealing that all elements are still uniformly distributed without obvious element separation and etching.

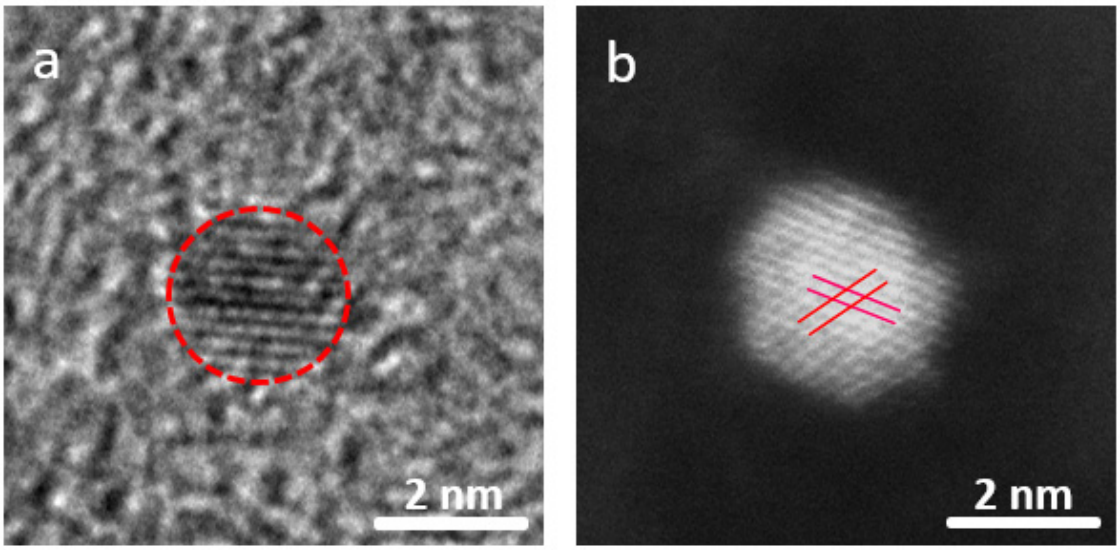

Supplementary Figure 26. The bright field (a) and dark field (b) TEM images of lattice fringes of us-HEA NPs after stability test, fully demonstrating that the NP can maintain a good crystal structure.

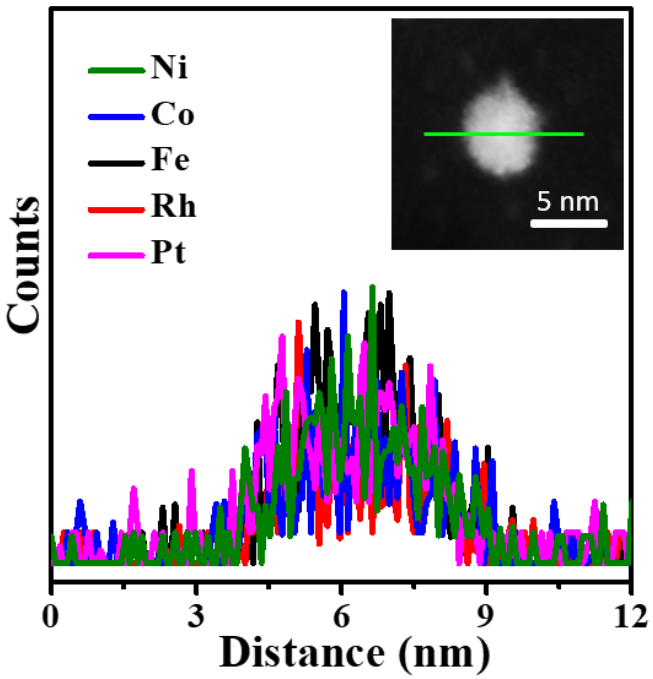

Supplementary Figure 27. The line scanning profiles of a single us-HEA NP after stability test, revealing that all five elements are still uniformly distributed and well-mixed without obvious element separation.

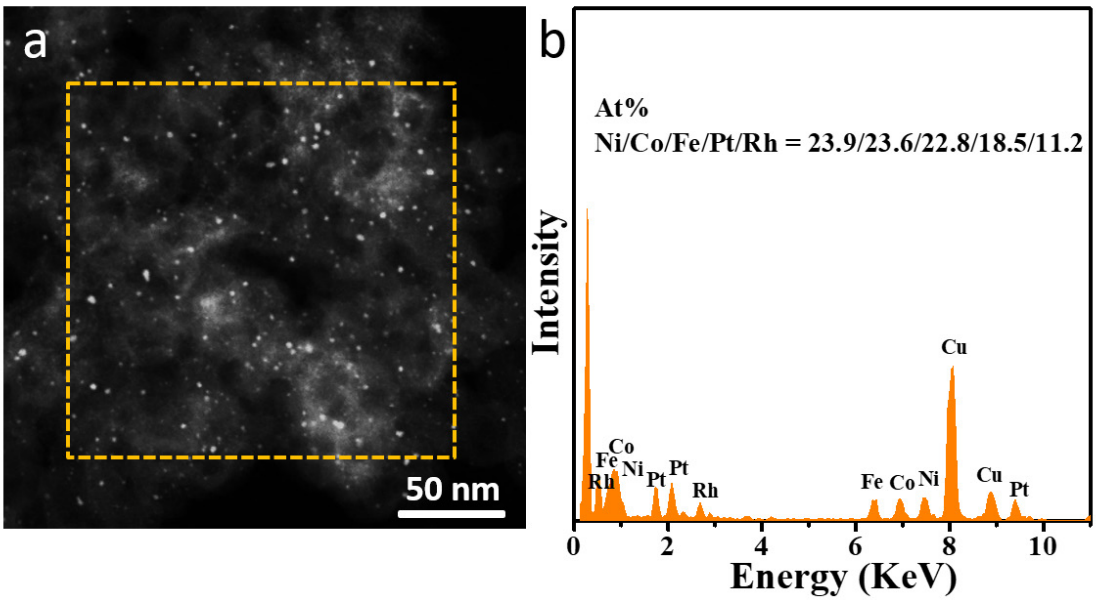

Supplementary Figure 28. EDS spectrum of lots of nanoparticles, demonstrating that five metals in us-HEAs can maintain compositions well without substantial composition loss after the harsh stability test.

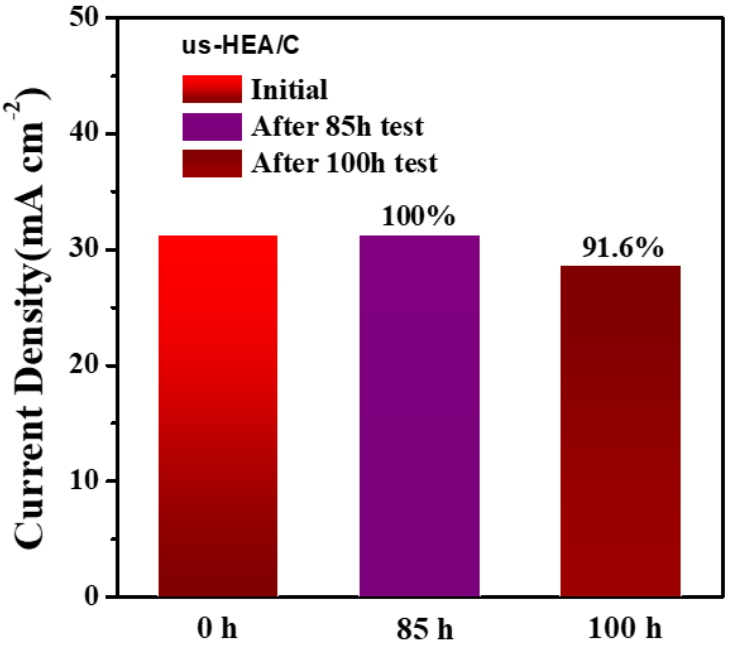

Supplementary Figure 29. Quantitative comparison of the current densities of us-HEA/C before and after constant applied potential for 85h and 100 h.

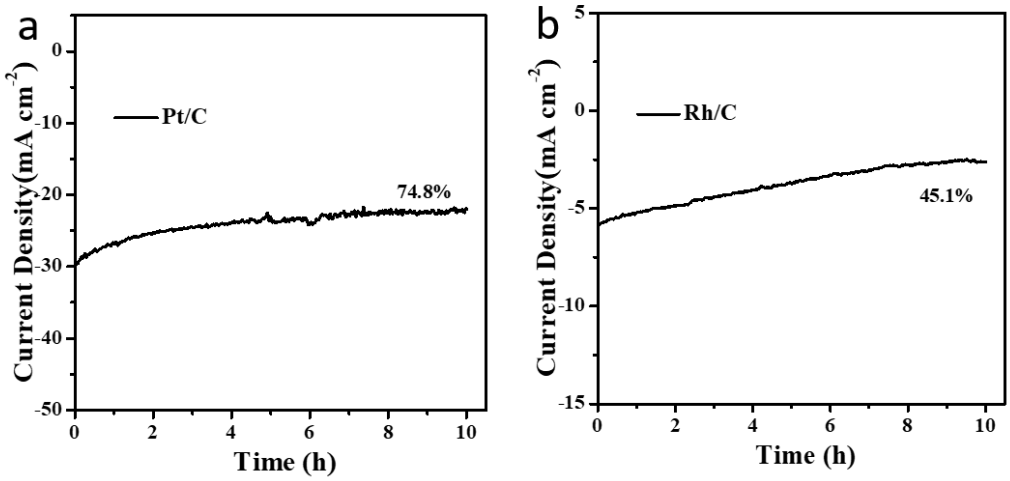

Supplementary Figure 30. Stability tests of commercial Pt/C (**a**) and Rh/C (**b**) through constant applied potential for 10 h, respectively.

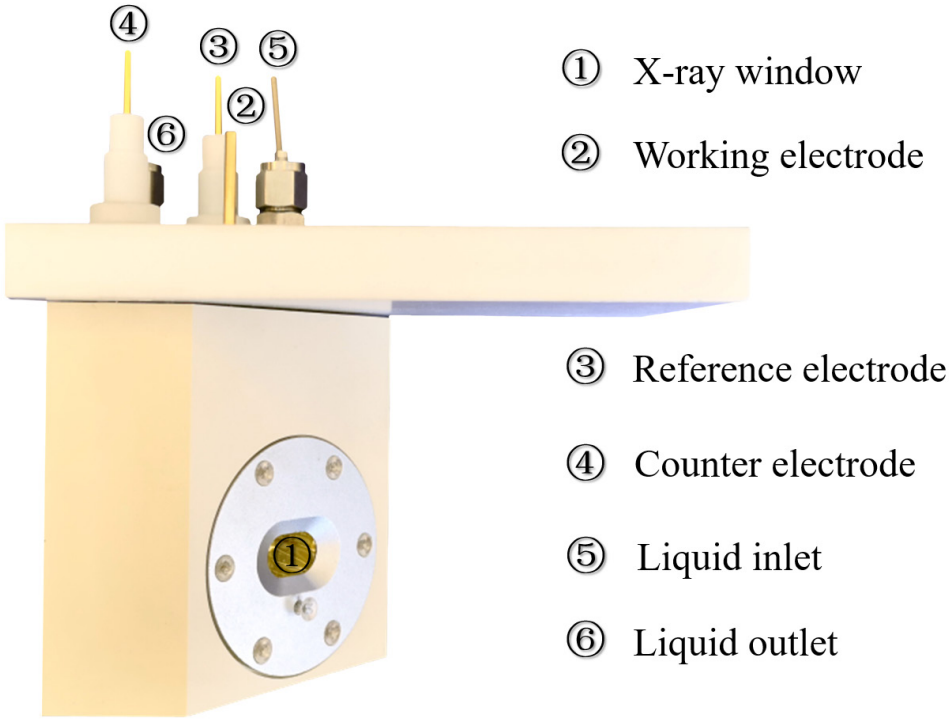

Supplementary Figure 31. Digital photograph of the operando fluorescence cell.

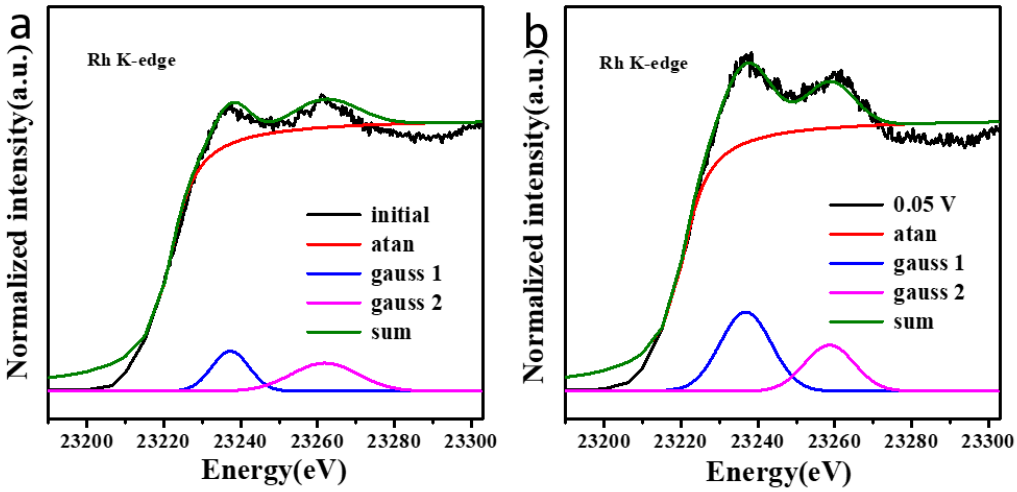

Supplementary Figure 32. De-convolution of in-situ Rh K-edge XANES of us-HEA/C recorded at different chemical states.

Supplementary Table 6. Amplitude and position of the main two XANES features at Rh K-edge at initial state and voltage-applied ones.

state	peak	position	amplitude (area)	Ratio (P2/P1)
Initial	P1	23237 eV	1.779	1.254
	P2	23260 eV	2.231	
0.05 V	P1	23237 eV	4.815	0.564
	P2	23260 eV	2.716	

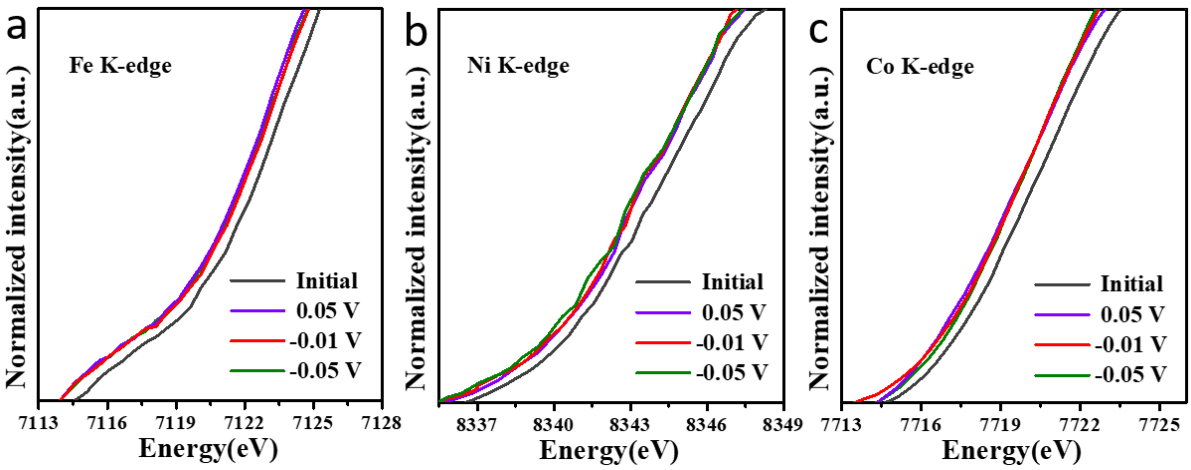

Supplementary Figure 33. Enlarged view of operando XANES spectra of us-HEA/C at Fe K-edge (**a**), Ni K-edge (**b**), and Co K-edge (**c**).

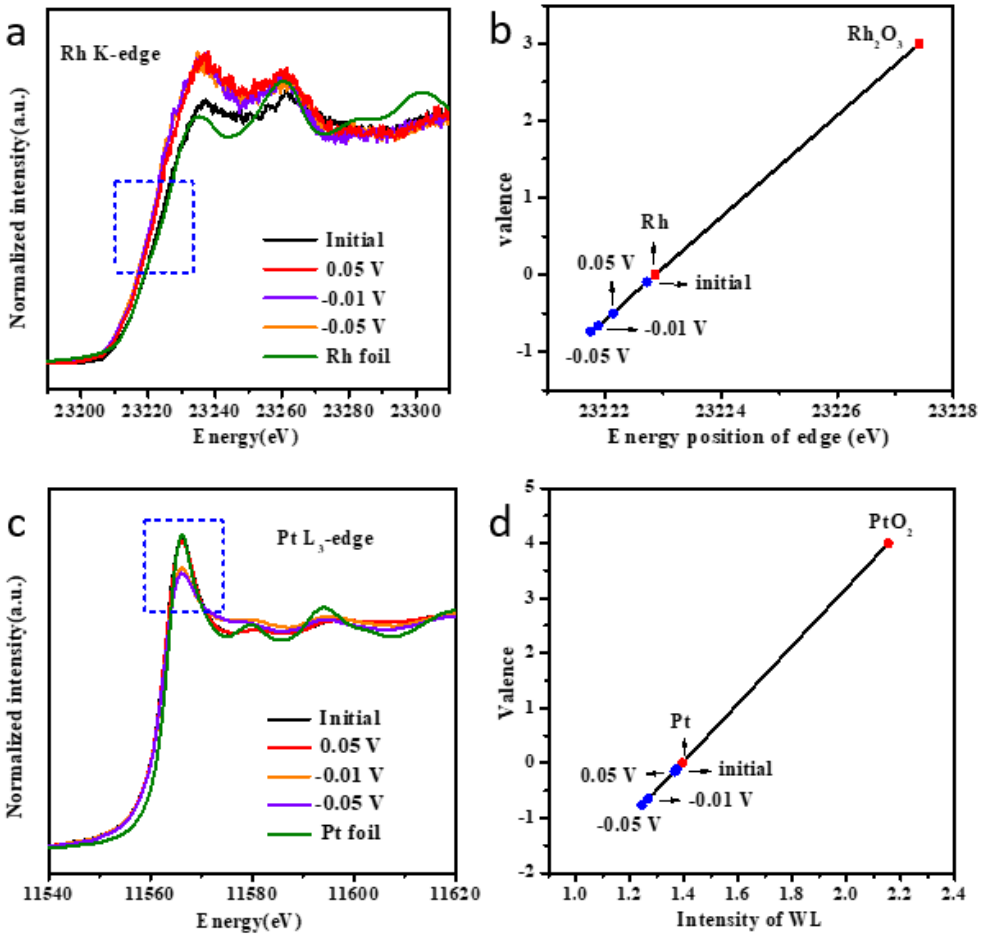

Supplementary Figure 34. Operando Rh K-edge (a) and Pt L_3-edge (c) XANES and the linear relationship of oxidized on Rh and Pt sites with the edge position (b) and the WL intensity (d), respectively.

It can be found that the valence states of both Rh and Pt at the initial state were a little lower than those of their elemental metals, demonstrating that Rh and Pt sites in the sample were still in the metallic state, rather than the oxidation state, achieving some electrons from their massively coordinated Fe/Co/Ni. When the cathodic potential of 0.05 V (no HER occurs) was applied, the valence state of Rh dramatically dropped compared to the initial state. It indicates that Rh gained numerous electrons, while a large number of hydrogen ions were adsorbed on the surface of Rh sites. In this case, the valence state of Pt changed a little. With the increase in the applied potential to -0.01 V and -0.05 V, the valence state of Rh continued to drop slightly. In contrast, the Pt dropped sharply when HER begins (-0.01 V), which illustrates that Pt sites are the dominant active sites for HER at this state. The above results demonstrate that the changes of the edge position for Rh XANES and the WL intensity for Pt one are mainly ascribed to the charge transfer between metals and reactants.

Supplementary Table 7. Three types of representative sites on us-HEA (111) surfaces at monolayer H coverage (θ_{H^*} =1).

Sites	H*-Case	ΔG_{H^*} (eV)
Rh site	H*-RhNiCo	-0.147
	H*-RhNiNi	-0.191
	H*-RhFeCo	-0.201
	H*-RhCoCo	-0.216
Pt site	H*-PtNiFe	-0.004
	H*-PtNiFe	-0.010
	H*-PtNiCo	-0.030
	H*-PtCoFe	-0.046
Fe/Co/Ni site	H*-FeCoNi	-0.127
	H*-FeCoNi	-0.152
	H*-CoNiNi	-0.160
	H*-CoFeFe	-0.177

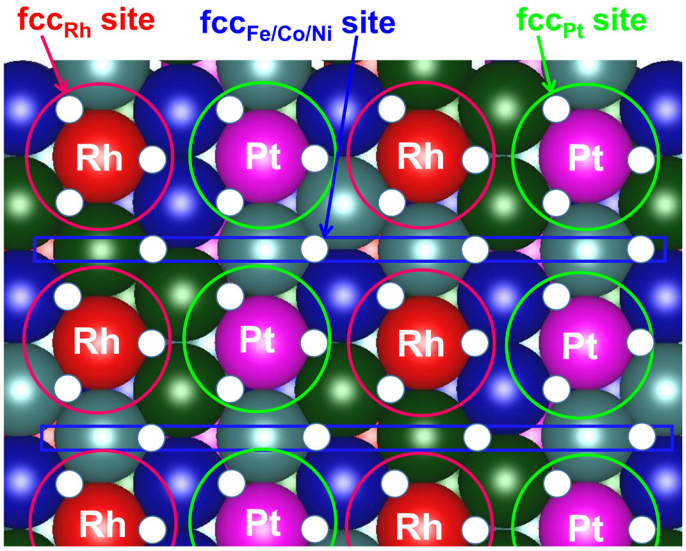

Supplementary Figure 35. Diagram of corresponding adsorption sites on the us-HEA (111) surface. The red, purple, green, blue, and cyan spheres are Rh, Pt, Fe, Co, and Ni atoms, respectively.

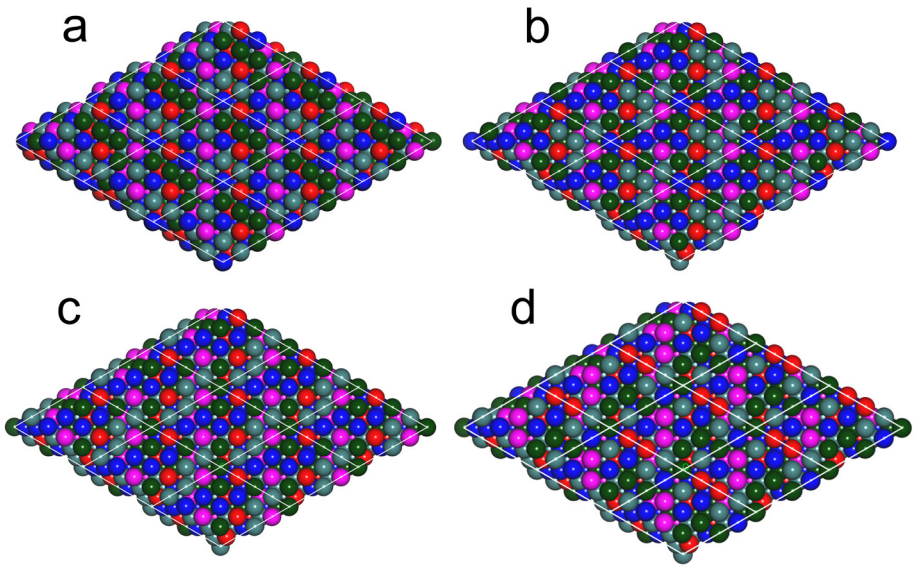

Supplementary Figure 36. Structural models with different atomic distributions of HEA. (a-c) different Fe/Co/Ni distributions and the Pt/Rh atoms are uniformly distributed. (d) Pt/Rh atoms are directly bonded. The red, purple, green, blue, and cyan spheres are Rh, Pt, Fe, Co, and Ni atoms, respectively.

According to the EXAFS results, the structural model of HEA (111) surface system based on uniformly distributed Pt/Rh atoms is reasonable.

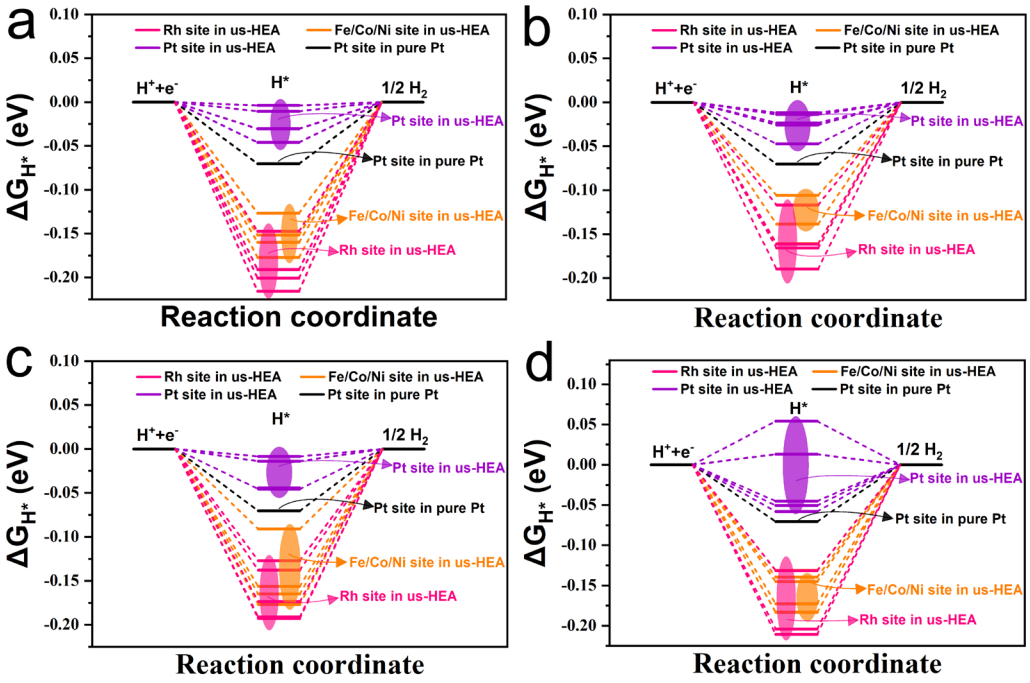

Supplementary Figure 37. The calculated hydrogen adsorption free energy (ΔG_{H^*}) profiles at high hydrogen coverage (θ_{H^*}=1) for three representative sites on us-HEA (111) surface based on four different structural models. (a-c) different Fe/Co/Ni distributions and the Pt/Rh atoms are uniformly distributed. (d) Pt/Rh atoms are directly bonded.

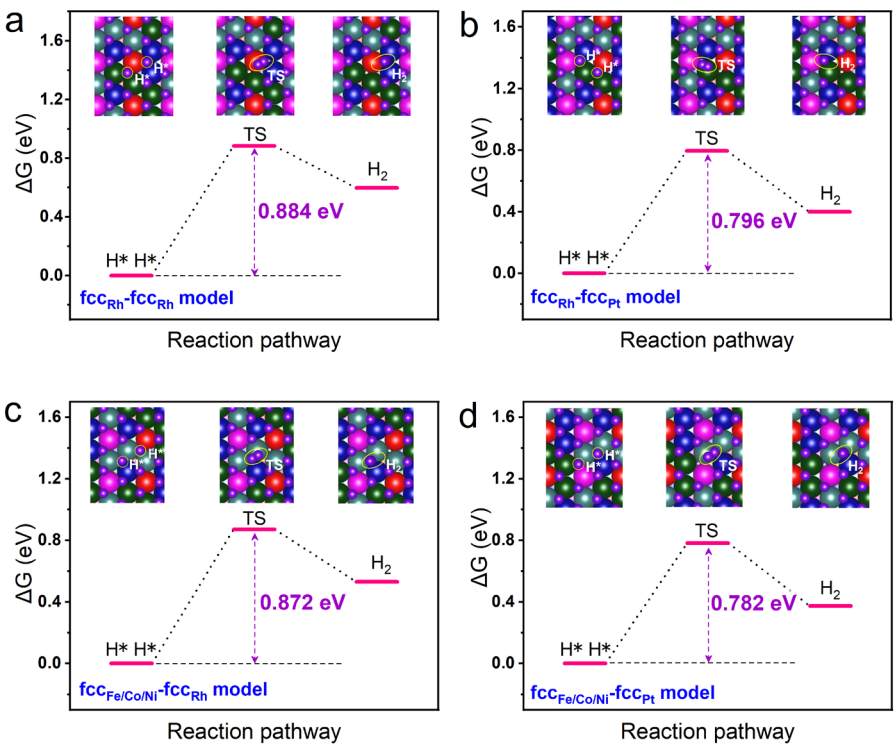

Supplementary Figure 38. The free energy diagrams of the Tafel reaction on the us-HEA (111) surface for fcc_{Rh}-fcc_{Rh} model (a), fcc_{Rh}-fcc_{Pt} model (b), $fcc_{Fe/Co/Ni}$-fcc_{Rh} model (c), and $fcc_{Fe/Co/Ni}$-fcc_{Pt} model (d).

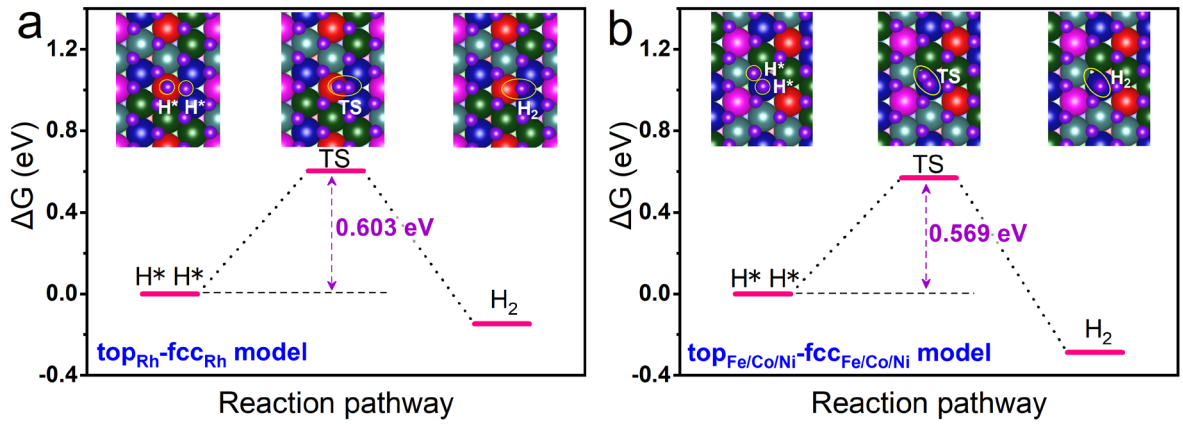

Supplementary Figure 39. The free energy diagrams of the Tafel reaction on the us-HEA (111) surface for top_{Rh}-fcc_{Rh} model (a), and $top_{Fe/Co/Ni}$-$fcc_{Fe/Co/Ni}$ model (b).

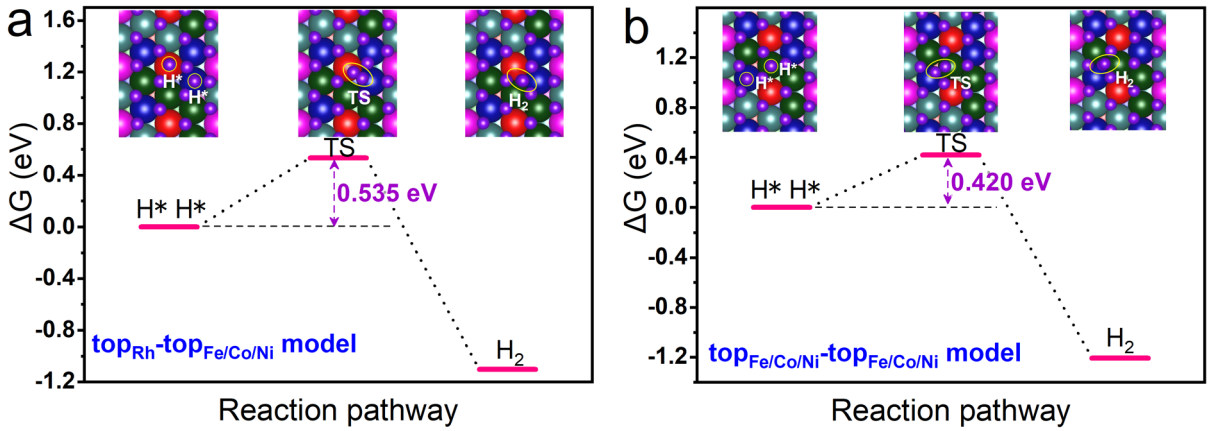

Supplementary Figure 40. The free energy diagrams of the Tafel reaction on the us-HEA (111) surface for top_{Rh}-$top_{Fe/Co/Ni}$ model (a), and $top_{Fe/Co/Ni}$-$top_{Fe/Co/Ni}$ model (b).

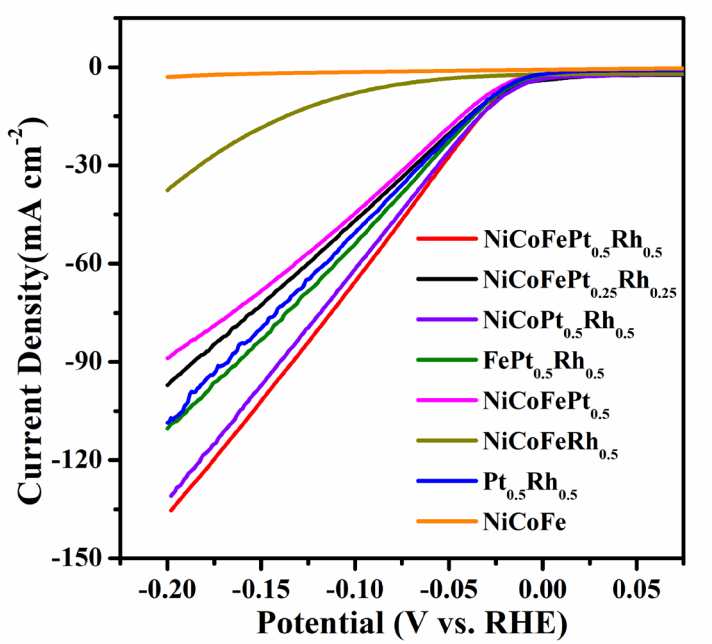

Supplementary Figure 41. Specific activities of the $Ni_xCo_yFe_zPt_uRh_v$/C for HER in 0.5 M H_2SO_4 solution without iR compensation ($NiCoFePt_{0.5}Rh_{0.5}$/C is the us-HEA mentioned in this work), indicating that there is a synergistic effect among the five elements and all five elements contribute to the enhanced HER performance together. Meanwhile, Pt and Rh play much more important roles than Ni/Co/Fe in catalytic performance. Furthermore, Pt is the most important role among five elements. The above results are in agreement with the DFT calculations and operando XAS results.